

Statistical Measures of Planck Scale Signal Correlations in Interferometers

Craig J. Hogan

University of Chicago and Fermilab Center for Particle Astrophysics

Ohkyung Kwon

University of Chicago

A model-independent statistical framework is presented to interpret data from systems where the mean time derivative of positional cross correlation between world lines, a measure of spreading in a quantum geometrical wave function, is measured with a precision smaller than the Planck time. The framework provides a general way to constrain possible departures from perfect independence of classical world lines, associated with Planck scale bounds on positional information. A parametrized candidate set of possible correlation functions is shown to be consistent with the known causal structure of the classical geometry measured by an apparatus, and the holographic scaling of information suggested by gravity. Frequency-domain power spectra are derived that can be compared with interferometer data. Simple projections of sensitivity for specific experimental set-ups suggests that measurements will directly yield constraints on a universal time derivative of the correlation function, and thereby confirm or rule out a class of Planck scale departures from classical geometry.

I. INTRODUCTION

Although it is widely believed that the world follows quantum principles, it is not known how classical dynamical space-time emerges from a quantum mechanical system[1, 2]. Standard field theory, often regarded as the basis of a fundamental quantum theory, encounters well-known, unavoidable divergences at the Planck scale[3–5]. The divergences may be avoided in a theory based on other fundamental objects such as strings[6–8], loops or spin networks[1, 2], and/or noncommutative geometries[9]; these theories can even lead to predictions of new behavior at the Planck scale, such as quantization of volume or area. However, for large systems, many issues remain unresolved, for example, the foundational inconsistency of quantum theory with the “local realism” associated with classical geometrical paths and events[10–12], the holographic encoding of information in dynamical gravitational systems, particularly black holes[13–22], and unphysically large masses of some field systems in large volumes[23, 24].

Most theoretical attention has concentrated on the ultraviolet part of the problem—the Planck scale regime dominated by string theory. On the other hand, the large-scale or infrared paradoxes also presumably arise because field theory is quantized on a fixed classical background, whereas the real space-time system emerges, along with the classical notion of locality, from a quantum system based on a Planckian bandwidth limit or discrete structure. While ultraviolet effects at the Planck scale cannot be measured directly, scaling from standard quantum mechanics suggests that indirect effects of Planck scale physics may be detectable in certain kinds of measurements in laboratory systems via spreading of geometrical position states over macroscopic distance.

Correlations signifying departures from perfect classical space could plausibly appear, according to standard quantum mechanics, on a scale given by diffraction of Planck frequency radiation propagating across an apparatus, or equivalently, the quantum position uncertainty of a Planck mass particle over a duration corresponding to an apparatus light-crossing time[24–28]. Field theory assumes a classically coherent background geometry, and predicts that such nonlocal quantum correlations of the background should be negligible.

Although the approximate magnitude of the correlations can be guessed from scaling, their detailed character is not known. In the absence of a standard theory for large systems in emergent geometry, in this paper we take an empirical, experimental approach to the problem. We ask, what can precise laboratory measurements of the relative positions of massive bodies at rest tell us about the character of positional information contained in the space-time itself, and in particular, the detailed degrees of freedom of the quantum system that gives rise to space and locality? We focus on what can be learned about the emergence of classical positions in space from the best available technique for nonlocal measurement of position, interferometry[29].

The predictions of any quantum theory are expressed in terms of correlations between observables. In the case of a space-time built from a quantum system, departures from classicality should appear in time-averaged correlations of positions of massive bodies. For a given configuration of massive bodies—for example, the mirrors in an interferometer—the forms that the correlation functions can take are constrained by general principles of symmetry and causality of the emerged space. We argue here that possible forms can be classified and evaluated from the known structure of a macroscopic apparatus, without knowing the elements and dynamics of the underlying quantum space-time degrees of freedom.

As one example of an observable correlation, signals from a pair of interferometers can be combined into a correlation function, whose mean time derivative has the dimension of time. If that has a value of the order of the Planck time, the information content of the measured spatial relationships is comparable with the total information content suggested by holographic bounds on entropy[25–28]. Interferometers are now close to achieving measurements of coherence with Planck precision, so the framework presented here can be used to interpret their signals in terms of Planck scale bounds on information.

The goal is to use data to test a general hypothesis: that geometrical information about directions between world lines in space, defined by measurements of the position of massive bodies with electromagnetic waves, obeys Planck scale covariant constraints on information. With the framework presented here, statistical properties of data in a broad class of experiments can be compared with each other, and used to test specific forms of this general hypothesis, even in the absence of a specific fundamental theory. Experiments can explore and constrain any form of Planckian correlations in space-time position consistent with symmetries imposed by the causal structure of the emergent system.

We apply our framework here to a particular kind of apparatus, a correlated pair of Michelson interferometers, such as the Fermilab Holometer[30], and also discuss how it can be generalized. In previous work[25–28], specific models of holographic spatial position states were used to predict properties of measurable “holographic noise” in interferometers. The more general framework here allows a broader class of quantum models to be tested, even some with no corresponding classical interpretation. In all cases, the coherence is characterized by a key universal parameter: the time derivative of a measured correlation function, normalized to the size of an apparatus. We propose two schemes that span the range of possible models, each of them characterized by two universal parameters of the order of the Planck time, that can be directly constrained by data.

Of course, different experimental set-ups, with different causal relationships between the world lines of their optical elements, will constrain Planckian departures from classical coherence in different ways. We do not exhaust all those possibilities here, but general principles of this framework can be extended to compare them with each other and with predictions of proposed theories. For example, the Michelson systems considered here measure only correlations spatially related by shear or strain transformations; they do not measure the important independent modes corresponding to pure rotations. Those modes, and apparatus that could measure them, will be treated in later work.

II. GENERAL FRAMEWORK

A. Scaling of Geometrical Correlations

Causal diamonds are defined as the 4-volume of spacetime over which an observer (defined by a timelike world-line) can do experiments. It is bounded by two null light-cones connecting two points on the observer’s world-line that are timelike separated (see Figure 1). A world line defines a causal diamond associated with any proper time interval of duration τ . It has been proposed that nested sequences of causal diamonds— covering increasing intervals along a timelike trajectory— correspond to sequences of nested Hilbert spaces[12, 31]. These causal diamonds serve as reference boundaries for geometrical information.

Consider an observable operator \hat{x} , with the dimension of length, that characterizes a set of world lines in some extended 4D volume of flat space-time. In general, a measurement of \hat{x} requires nonlocal propagation of light within a causal diamond; it represents a projection of an extended 4D quantum system. In the interferometer systems considered here, an observable signal depends on the world lines of an arrangement of mirrors, and encodes nonlocal information about their positions and about the state of the laser field. Here, we ignore these standard quantum degrees of freedom; the operators \hat{x} measure new noncommuting degrees of freedom that differ from the standard motion[32] of a massive body in a classical geometry. A measurement of \hat{x} represents a measurement of positional degrees of freedom that are assumed to be classical in the standard quantization of fields and optical elements in an interferometer[33, 34]. They correspond to new degrees of freedom associated with the nonclassical character of emergent world lines; thus, we know neither the Hamiltonian nor the conjugate operators for \hat{x} . (Other forms of entanglement with Planck scale geometrical states have been discussed in ref. [35].) The value of \hat{x} does not depend on the masses or other properties of bodies, only on their relative positions.

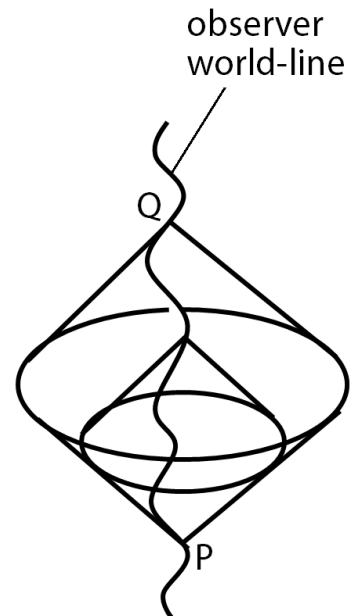


FIG. 1. Causal diamonds.

Suppose that the measured value of \hat{x} departs by some amount $\Delta x = \hat{x} - \bar{x}$ from its expected value \bar{x} in classical space-time. A measure of the deviation from perfect classical coherence is given by a time-domain correlation function of the form,

$$\Xi(\tau) \equiv \langle \Delta x(t) \Delta x(t + \tau) \rangle_t F(\tau). \quad (1)$$

Here, $F(\tau)$ denotes a projection determined by the configuration of a measurement apparatus. In general, correlations can be measured for two world lines, say \hat{x}_A and \hat{x}_B ; most of this paper focuses on the configurations where A and B causal diamonds are almost the same.

The positional correlation encoded in Ξ measures a lack of independence of values of \hat{x} . In a classical space-time, Ξ vanishes; this is possible because the information density in a continuum is infinite. The same is true in field theory, which assumes a classical continuous space-time. In an emergent quantum space-time, Ξ in general does not vanish, and the positions of world-lines in some measurements can decohere gradually with time. The 2D density of position eigenstates—that is, the number of independent world-line eigenstates per 2-volume in a particular \hat{x} projection—has a finite value given by Ξ^{-1} . Its value depends on the projection defined by the measurement, and the invariant classical positional relationships between the world lines, particularly the causal diamonds traced by light propagation in the apparatus.

The scaling with τ can be estimated from dimensional considerations, or from analogy with other, standard quantum systems. It is plausible that world lines decohere slightly at long durations, by an amount that would not yet have been detected. As one example of a quantum system with this behavior, consider the standard position wave function for the state of a particle of mass m at rest, that lasts for duration τ . This form of standard Heisenberg uncertainty can be derived in several ways[24–27], for example from a nonrelativistic Schrödinger equation for a mass m , in a path integral approach by extremizing the action of a particle or body whose motion is described by a wave equation with de Broglie wavelength \hbar/mc , or from a Wheeler-De Witt equation for a pendulum of mass m in the low frequency, nearly free particle limit. For all of these systems, with the standard assumption that directions in space are independent, the wave function in classical position and time obeys

$$(\partial_i \partial^i - 2i(m/\hbar)\partial_t)\psi = 0. \quad (2)$$

This equation can be solved with pure (infinite) plane wave eigenmodes. However, the state of a body localized in space, whose position is prepared and measured at two times separated by an interval much longer than the inverse de Broglie frequency, is better described by a symmetric gaussian solution for $\psi(r, t)$, where $r^2 = x_i x^i$, with a probability density on constant-time surfaces given by

$$|\langle \psi^* | \psi \rangle|^2 \propto e^{-r^2/\sigma(t)^2}. \quad (3)$$

These “paraxial” solutions for matter de Broglie waves are mathematically the same as the standard normal modes of light[36] in a laser cavity. In the matter system, t takes the place of the laser beam axis coordinate z (that is, constant-phase de Broglie wavefronts are nearly surfaces of constant time), and position measurements at particular times, over an interval much smaller than the interval between measurements, takes the place of thin mirror surface boundary conditions[24]. In this family of solutions, the rate of spatial spreading depends on the preparation of a state: $d\sigma/dt$ is smaller for larger σ . In the same way that a larger beam waist leads to a smaller dispersion angle, a larger position uncertainty leads to slower spreading. Spreading of the wave function with time is unavoidable; any solution of duration τ has a mean variance of position at least as large as

$$\langle (r(t + \tau) - r(t))^2 \rangle = \sigma_0^2(\tau) > \hbar\tau/2m. \quad (4)$$

Thus, $d\sigma_0/d\tau = \hbar/2m$ gives the minimum rate of spreading in the position state of a body at rest over time.

Of course, these states also have an associated indeterminacy of momentum. Although the particle is classically “at rest”, and there is a well defined expectation value for its rest frame, the actual velocity is indeterminate. In this situation, the position variance between two times cannot be “squeezed away” into momentum uncertainty, or vice versa; Eq. (4) gives the minimum spread of position between two times for *any* state[33, 37]. The momentum uncertainty in the minimum-position-uncertainty state decreases with τ like $\Delta p \approx (2m\hbar/\tau)^{1/2}$, which is why de Broglie wave states behave almost like classical world lines on large scales.

Similarly, if paths in a background quantum space time are described by quantum wave propagation similar to Eq. (2), with a fundamental timescale set by the Planck time (that is, setting $m = m_P = \hbar/c^2 t_P$), then its emergent world line states spread over duration τ by about

$$\Xi(\tau) \approx \langle (x(t + \tau) - x(t))^2 \rangle \approx c^2 \tau t_P / 2. \quad (5)$$

To be sure, this background spreading cannot be detected by a local measurement, in the same way that quantum decoherence between independent paths of mass m_P bodies can be measured by comparing their positions, because the geometrical states of nearby world lines are entangled with each other. It may also include exotic correlations between different directions and components of position, which we have not included. However, the scaling of $\sigma_0^2(\tau)$ and $\Xi(\tau)$ with τ are the same: world lines should decohere at a rate given approximately by $d\Xi/d\tau \approx c^2 t_P/2$.

For large systems (that is, $\tau \gg t_P$), the variance of position is much larger than the typical value $\Xi \approx c^2 t_P^2$ from Planck scale field fluctuations on a classical background. At the same time, the variance is very small, and the trajectories behave nearly classically. Because the deviation can only be seen in a highly precise nonlocal measurement of correlations, it would not have been detected in previous experiments. A 100m laboratory scale experiment is $\approx 10^{37}$ Planck lengths across; Planckian spreading on the corresponding timescale ($10^{37} t_P \approx 10^{-6}$ sec) is only $\approx 10^{18.5} c t_P \approx 10^{-16.5}$ meters, and the typical variation in rest frame velocity is about $\approx 10^{-18.5} c$, or a few mm per year—an order of magnitude slower than continental drift.

The same scaling is suggested by applying holographic bounds to information in the relative position of world lines. The holographic principle posits covariantly that the information \mathcal{I} in a causal diamond of duration τ is one quarter of the area of its bounding surface in Planck units, or $\mathcal{I}_H = (\pi/4)(\tau/t_P)^2$ in flat space. Suppose that the position operator \hat{x} depends on positions distributed over a 3-volume $\approx (c\tau)^3$, and that the density of information in the radial dimension of the causal diamond has some value ℓ_r^{-1} in its rest frame, independent of system size. The number of position states is then $\mathcal{I}_x \approx (c\tau)^3 \ell_r^{-1} \Xi^{-1}$. If we require that $\mathcal{I}_x < \mathcal{I}_H$, so that the holographic information bound applies to spatial information, we obtain

$$\Xi(\tau) > \tau(c^3 t_P^2 / \ell_r)(\pi/4). \quad (6)$$

Thus, there is some universal value of $\dot{\Xi} \equiv d\Xi/d\tau$ associated with holographic scaling of position information. Since the natural value of ℓ_r is of order $c t_P$, the natural value for $\dot{\Xi}$ is again of order $c^2 t_P$.

The value of $\dot{\Xi}$ depends on the configuration of the world lines represented in the operator \hat{x} . For some \hat{x} operators that do not measure degrees of freedom where the information is bounded, it may vanish by symmetry; that is, the uncertainty could be squeezed into unmeasured degrees of freedom. Although the analogy (Eq. 2) is suggestive of how solutions should scale, we do not know how measurements in different directions, or between different world lines, should relate to each other, or how the wave function should be interpreted physically. The experimental program is to measure correlations where we can, and perhaps uncover clues to the underlying theory.

The current exercise is to lay out statistical measures that can measure the value of $\dot{\Xi}$ with data from simple experimental setups. The form of Ξ can be constrained from general considerations about the causal diamonds corresponding to the arrangement of mirrors in an apparatus, so well-characterized universal conclusions about quantum geometry can be drawn from a specific experimental result.

B. Constraints on Correlations in Interferometer Signals

Consider two Michelson interferometers, A and B , with dark-port signals $x_A(t)$ and $x_B(t)$ calibrated in length units. The statistical quantity estimated from a time stream of data is a cross correlation between interferometers A and B :

$$\Xi(\tau) \equiv \langle x_A(t) x_B(t + \tau) \rangle. \quad (7)$$

The projection $F(\tau)$ (that is, the connection between the signal x and Δx in Eq. 1) has here been absorbed into the definition of the apparatus that produces the signal.

Classically, the signal x is the departure of the length difference between the two arms from the average value. In a static classical space-time with no physical coupling between the two interferometers and no gravitational waves, the average cross correlation vanishes, $\Xi = 0$. However, if the two interferometers share a volume of space-time—that is, if the causal diamonds traced by the propagation of light in their arms overlap in some way—a correlation might be induced by Planckian holographic bounds on the amount of positional information in the system measured by the two sets of optics. They may be entangled by geometrical states in a way that statistically correlates the measurements.

We now propose a simple framework to test the general holographic noise hypothesis: that there is a nonzero correlation between A and B due to entanglement of the emergent space measured by the two interferometers. This framework is formulated in a general way so that the statistical results of a specific experiment can be used to constrain any (future) candidate universal theory of quantum geometry.

Even without a specific fundamental theory, we know that holographic correlations (if they exist at all) are subject to a few simple mathematical and physical constraints.

1. $\Xi(\tau)$ must be symmetric, $\Xi(\tau) = \Xi(-\tau)$. Time symmetry and covariance dictate that $\Xi(\tau)$ must be either symmetric or antisymmetric. However, Parseval's theorem requires that $\Xi(\tau)$ must have a nonzero value at zero lag if there is to be any measurable fluctuation in a real-valued signal, eliminating the latter choice.

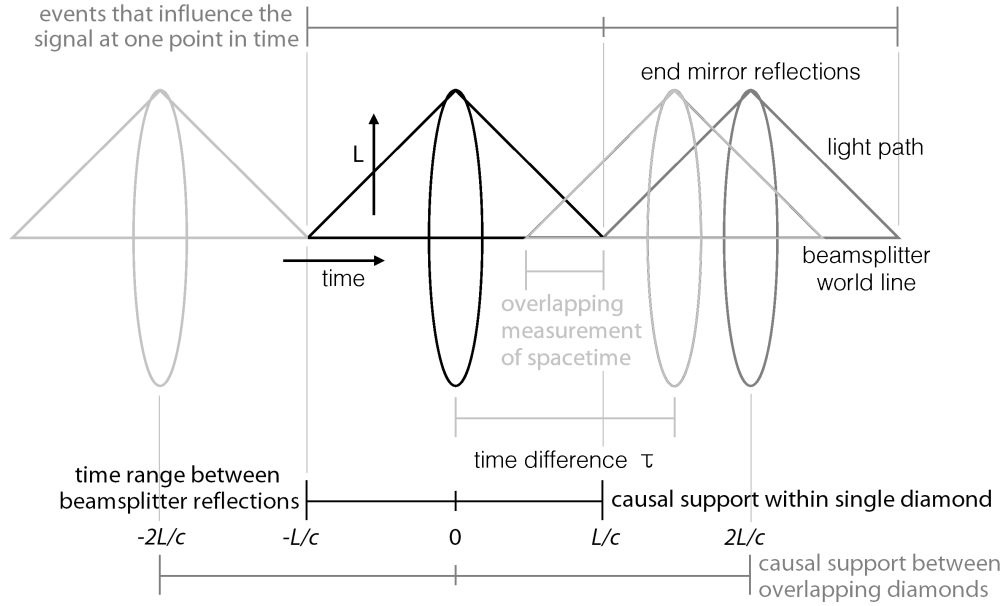


FIG. 2. A comparison of causal support in the two classes of correlation functions.

2. The correlation function must respect the causal region in the emergent space. For a simple configuration of two aligned Michelson interferometers with arm length L , we expect the functional support to be limited by the causal diamond to the interval $\tau = (-L, +L)$ between reflections on the beamsplitters, or the interval $\tau = (-2L, +2L)$ of events that influence the signal at any given time (see Figure 2). More general interferometer configurations may add additional scales, or even additional world-lines, and yield different functions.
3. The main hypothesis being tested is that relative positions of massive bodies as encoded in $\Xi(\tau)$ are subject to Planck scale spreading of information just described. Scaling symmetry then requires that where it does not vanish, $\Xi(\tau)$ is linear in τ , with a derivative $d\Xi/d\tau$ that does not depend on the size of the apparatus (see nested causal diamond in Figure 3). To match holographic information content, its absolute value is approximately the Planck time t_P . A more careful evaluation of numerical factors follows below.

With these constraints, for a given apparatus, candidate forms for $\Xi(\tau)$ are completely determined by two parameters. We consider below two possible forms for $\Xi(\tau)$ which span the range of consistent options. We also consider how the form of $\Xi(\tau)$ depends on the apparatus configuration—the sizes and relative positioning of two interferometers in space. The detailed worked examples here apply to configurations where the interferometers are adjacent, so that causal diamonds substantially overlap; the simple arrangement reduces the number of parameters needed to characterize the system.

III. PARAMETERIZED MODELS OF CORRELATION FUNCTIONS

Two broad classes of correlation functions respect the constraints just outlined. In both cases the models are described by two parameters that are universal physical constants, that according to the holographic noise hypothesis should not depend on apparatus size. The main difference is whether or not the correlation function goes continuously to zero at the lag corresponding to the edge of the causal diamond defined by the end mirrors. Figure 2 demonstrates the different causal support for the two classes. These two classes appear to span the space of possibilities consistent with the above constraints.

A. Models spanning $\pm L$

In the first class of models the correlation is allowed to jump discontinuously to zero. The two parameters are the zero lag value normalized to arm length $\Xi(\tau = 0)/L$,

$$\xi_0 \equiv \Xi(\tau = 0)/L, \quad (8)$$

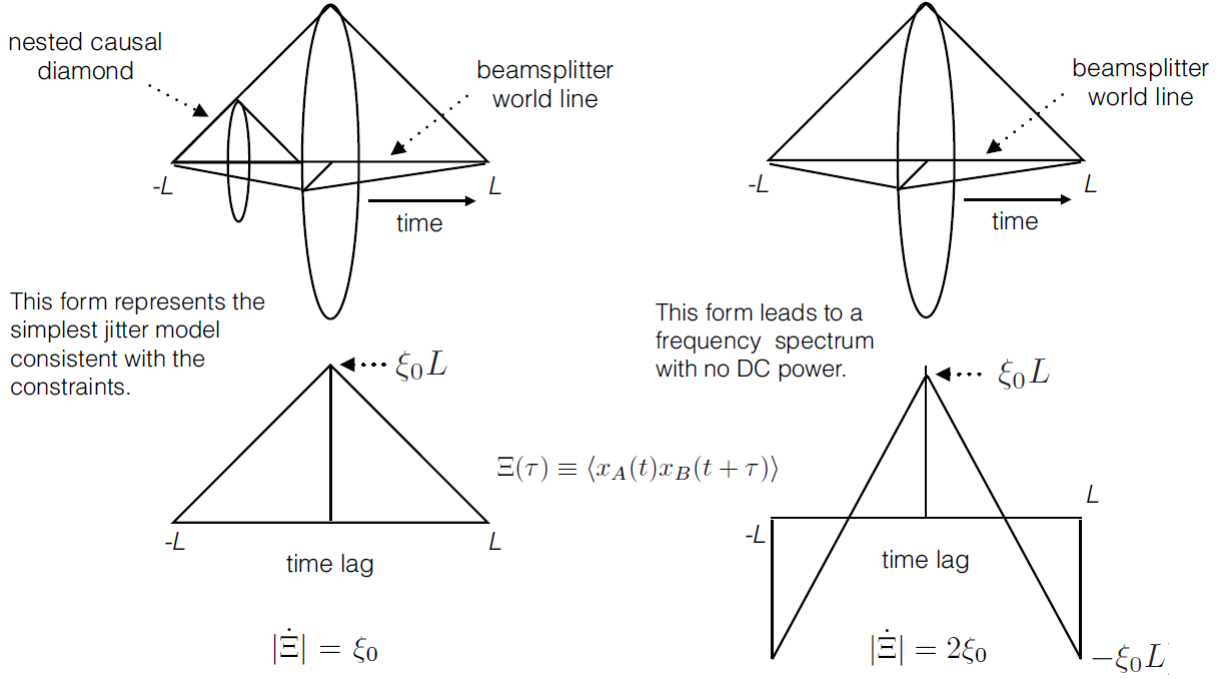


FIG. 3. Models spanning $\pm L$: Examples of time domain cross spectra.

and the norm of the derivative $|\dot{\Xi}|$. According to the holographic noise hypothesis, both ξ_0 and $|\dot{\Xi}|$ are of the order of the Planck time. A choice of ξ_0 and $|\dot{\Xi}|$ predicts a frequency spectrum that can be compared with Holometer data. A set of data can be used to generate joint likelihood contours for these two universal numbers.

The derivative is constrained by the causal diamond support constraint to

$$|\dot{\Xi}| > \xi_0. \quad (9)$$

If this bound is saturated (that is, $|\dot{\Xi}| = \xi_0$; see Figure 3), the holographic noise can be physically interpreted as a new kind of exotic “jitter” in space and in beamsplitter position. This is the kind of illustrative model considered in previous work[28], and used to estimate experimental sensitivity for design purposes.

A steeper slope is possible, in which case Ξ goes negative. This set of models generalizes the simple model of beamsplitter jitter; it requires more exotic nonlocal correlations in the causal 4-volume. For holographic noise, such a radical possibility should not be discounted *a priori*. However, for the integral $\int d\tau \Xi$ to be positive still requires the slope not to be too steep,

$$|\dot{\Xi}| < 2\xi_0. \quad (10)$$

If this bound is saturated (that is, $|\dot{\Xi}| = 2\xi_0$; see Figure 3), there is no DC power in the frequency spectrum, because the integral of Ξ vanishes.

Analytically, given two parameters ξ_0 and $|\dot{\Xi}|$, the frequency domain power spectrum is:

$$\tilde{\Xi}(f) = 2 \int_0^{L/c} (\xi_0 L - |\dot{\Xi}|\tau) \cos(2\pi f\tau) d\tau \quad (11)$$

$$= \frac{2|\dot{\Xi}|}{(2\pi f)^2} \left[1 - \cos\left(\frac{f}{c/2\pi L}\right) \right] - \frac{2}{2\pi f} \left(\frac{L}{c}\right) (|\dot{\Xi}| - c\xi_0) \sin\left(\frac{f}{c/2\pi L}\right) \quad (12)$$

$$= \left(\frac{L}{c}\right)^2 \left[|\dot{\Xi}| \text{sinc}^2\left(\frac{f}{c/\pi L}\right) - 2(|\dot{\Xi}| - c\xi_0) \text{sinc}\left(\frac{f}{c/2\pi L}\right) \right] \quad (13)$$

Figure 4 shows the type of spectra that are expected.

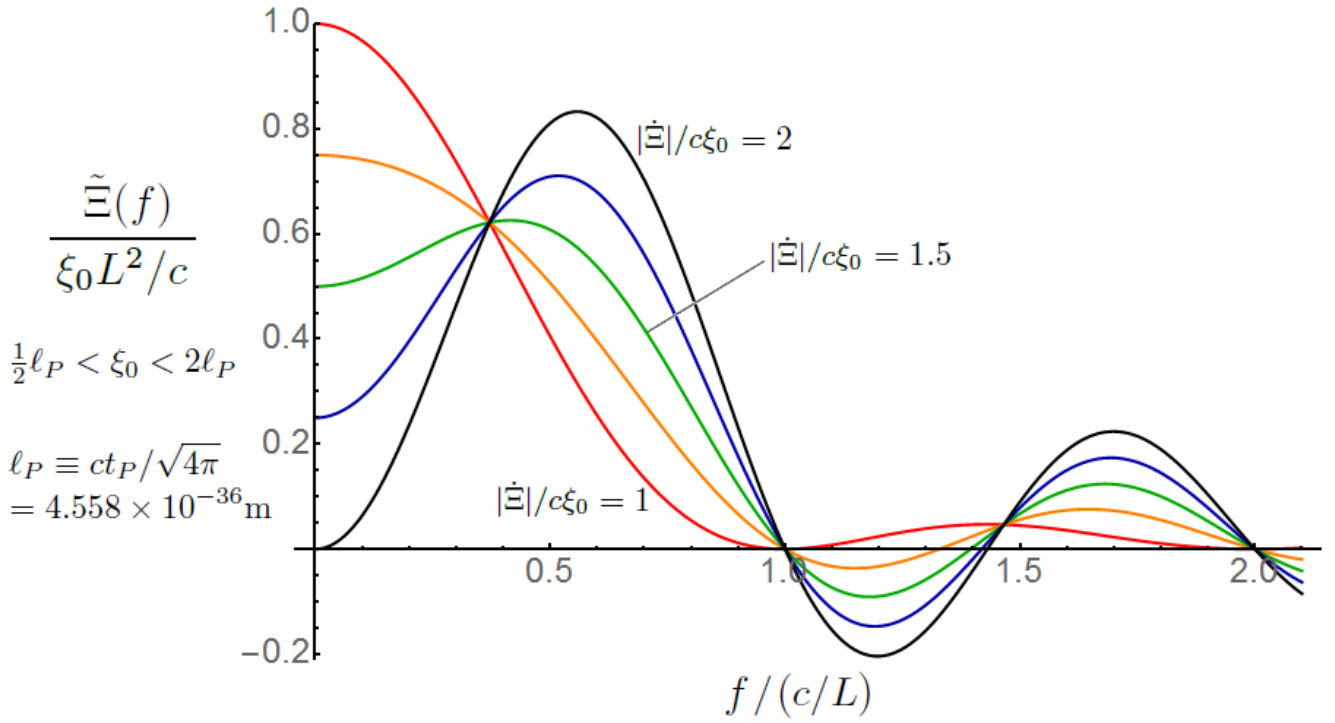


FIG. 4. Models spanning $\pm L$: Range of possible frequency domain spectra. Vertical axis is scaled relative to ξ_0 , which is on the order of the Planck scale. Horizontal axis is scaled to inverse light travel time for L . Five values of $|\dot{\Xi}|/c\xi_0$ linearly ranging from 1.0 to 2.0 are shown, corresponding to a horizontal line in Figure 5 (within the causally allowed region) for a single value of ξ_0 .

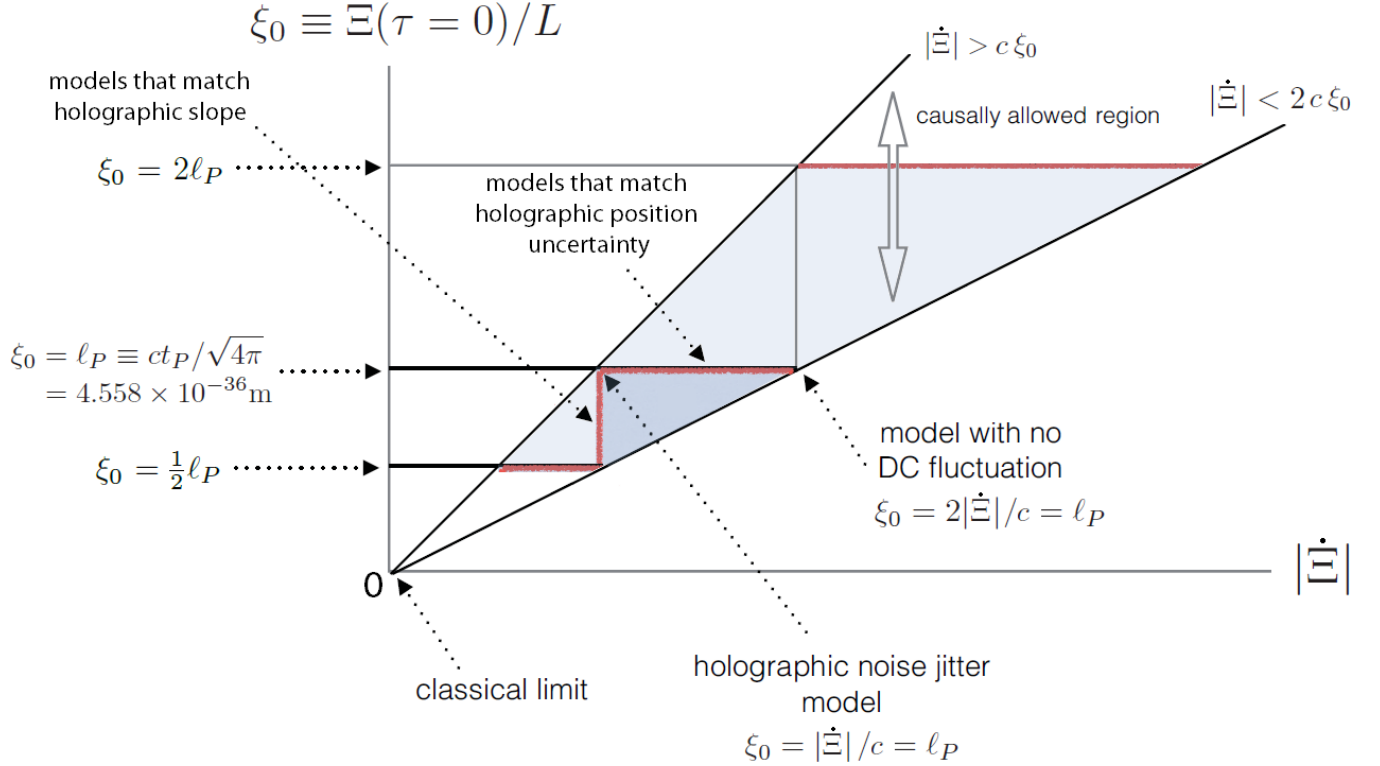


FIG. 5. Models spanning $\pm L$: Two observable length parameters span all possible models of noise that are consistent with symmetries of spacetime, causal structure, and holographic limits on geometric information (the shaded regions). The darker shaded triangle represents the region of parameter space bounded by our benchmark normalization.

Normalization from Holographic Gravity

A fundamental theory of emergent geometry should make an exact prediction for the parameters in correlation functions of a given apparatus. In the absence of such a theory, we adopt a specific benchmark for numerical values, normalized in a simple covariant model from the holographic principle. As shown in the appendix below, we fix the total number of states within distance L from holographic or “entropic” gravity. Then, a simple model based on a covariant antisymmetric commutator algebra connects the number of states with an exact universal numerical value for the transverse variance of a spatial wavefunction in physical length units, scaled to separation L :

$$\langle x_{\perp}^2 \rangle_L / L = \ell_P \equiv ct_P / \sqrt{4\pi} \equiv \sqrt{\hbar G / 4\pi c^3} = 4.558 \times 10^{-36} \text{m}. \quad (14)$$

This value sets a benchmark scale of the signal correlation function, $\Xi(\tau = 0)$, that saturates the holographic bound in a causal diamond of radius L .

Normalization for Measurable Correlated Noise: Upper and Lower Bounds

Equation (14) gives a reference scale for the transverse variance associated with distance L , but in order to predict the signal measured in interferometric experiments under this hypothesis, we must conduct a holistic analysis of a quantum-geometrical system of matter and light. It requires a full quantum theory that integrates the Hilbert space of photon states with those of emergent-geometric position states for the mass elements that comprise the optics. In the absence of such a theory, we will establish upper and lower bounds on ξ_0 , and therefore also on $|\dot{\Xi}|$ by the above constraints.

A benchmark for ξ_0 is when Eq.(14) and (8) are compared straightforwardly, i.e. $\xi_0 = \ell_P$. These describe models that match holographic position uncertainty. We expect the same benchmark for $|\dot{\Xi}|$ for models that match holographic slope, $|\dot{\Xi}| = \ell_P$.

The upper bound for ξ_0 is saturated when the measurements of two orthogonal arms lengths contribute independent uncorrelated parts to Ξ . We assume that the transverse variances from Eq.(14) directly apply to the beam splitter, as light beams make simultaneous measurements of orthogonal directions at this position.

$$\xi_0 < 2\ell_P \quad (15)$$

Note that we may not count the arm length L twice to account for the round trip time, because doing so while also counting two orthogonal arms would violate quantum limits on information. The holographic bound limits us to the size of the apparatus instead of the whole light path. This normalization is consistent with previous work [28].

The lower bound is saturated when the transverse variance from Eq.(14) is divided between the beam splitter and the end mirror, implying that the equivalent measurable position uncertainty at the beam splitter is halved. We also assume that holographic bounds on information limit the measurable noise to the transverse variance from the arm length in one direction, seeing the two orthogonal directions as noncommutative.

$$\xi_0 > \frac{1}{2}\ell_P \quad (16)$$

The region of parameter space allowed under the above constraints is summarized in Figure 5. The Holometer is expected to reach the sensitivity to detect or rule out all models that are physically allowed.

B. Models spanning $\pm 2L$

In this class of models, the causal support contains all events that influence the signal at a given time, and therefore the correlation does not discontinuously go to zero at the edge of a single causal diamond (representing a round trip to end mirrors, between reflections at the beam splitter). Instead, we consider the overlap between causal diamonds separated by τ , and maintain functional support for Ξ wherever the shared 4-volume is nonzero. We expect $\Xi(\tau)$ to be continuous at the edge of a single causal diamond and linearly fall off to zero at the edge of the causal limit.

See Figure 6. The left hand side shows how the overlap between two causal diamonds changes as the time lag between them increases. In a causal diamond describing an interferometer, the left half represents outgoing light propagating towards the end mirrors, and the right half represents incoming light coming back towards the beamsplitter. We use the term “parallel overlap” and “antiparallel overlap” to respectively denote ranges of time where the overlapping light path is parallel or antiparallel in 4-space.

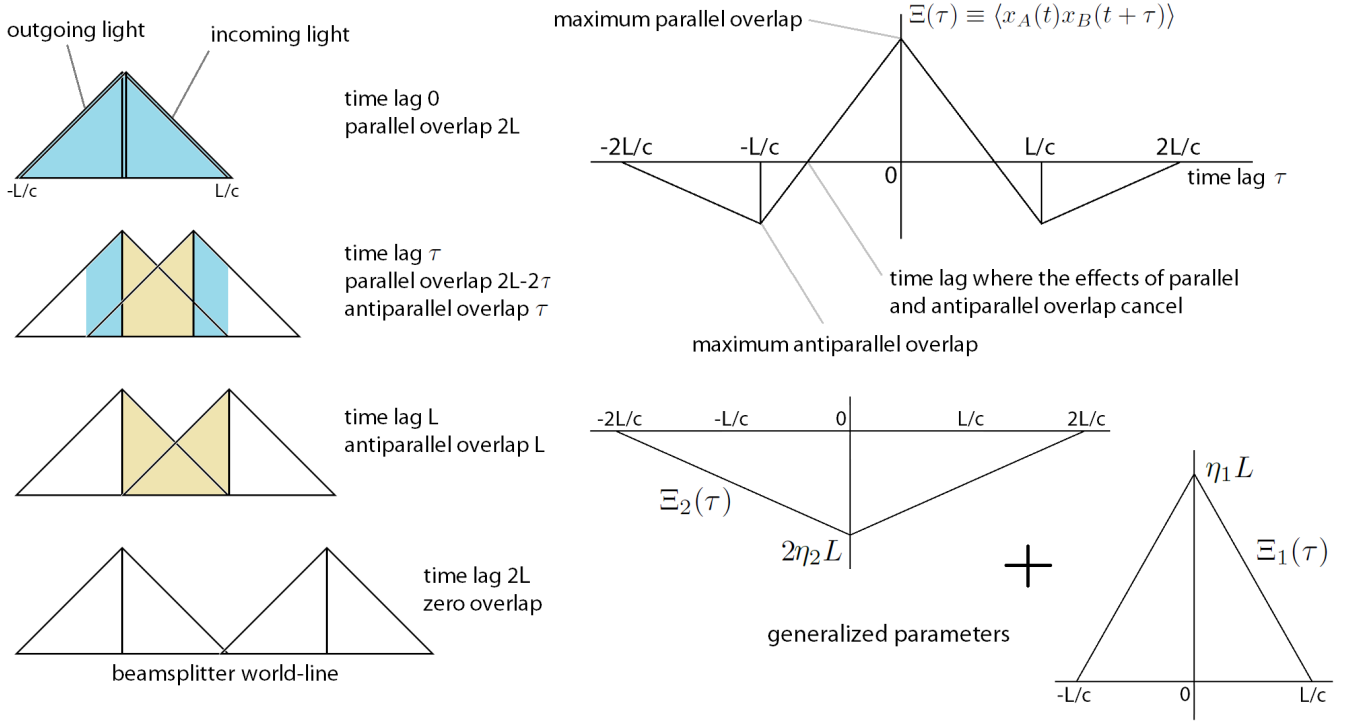


FIG. 6. Models spanning $\pm 2L$: Creating a generalized two-parameter space for possible correlation spectra.

If we assume that their contributions to $\Xi(\tau)$ are equally weighted and opposite in sign, at time lag $\tau = \frac{2}{3}L/c$, the amount of parallel overlap precisely cancels the antiparallel overlap. The top plot on the right hand side shows an example of $\Xi(\tau)$ under such assumptions. It is naturally a sum of the two plots below that, which define the generalized slope parameters $c\eta_1$ and $c\eta_2$ that establish the parameter space for this class of models. As before, both parameters are on the order of Planck time and not dependent on the apparatus size.

$$\Xi(\tau) = \Xi_1(\tau) + \Xi_2(\tau) \quad (17)$$

$$= \begin{cases} \eta_1(L - c|\tau|) & |\tau| < \frac{L}{c} \\ 0 & |\tau| > \frac{L}{c} \end{cases} + \begin{cases} \eta_2(2L - c|\tau|) & |\tau| < \frac{2L}{c} \\ 0 & |\tau| > \frac{2L}{c} \end{cases} \quad (18)$$

$$c\eta_1 \equiv \dot{\Xi}_1(-\frac{L}{c} < \tau < 0) = -\dot{\Xi}_1(0 < \tau < \frac{L}{c}) \quad \text{and} \quad c\eta_2 \equiv \dot{\Xi}_2(-\frac{2L}{c} < \tau < 0) = -\dot{\Xi}_2(0 < \tau < \frac{2L}{c}) \quad (19)$$

The two triangle functions, with causal support ranging to $\pm L/c$ and $\pm 2L/c$ respectively, each satisfies the condition for scaling symmetry established in the previous section. We interpret this to mean that we are proposing two ways in which nonlocal correlations can manifest in the emergent geometry, one that is fully contained within the causal 4-volume of a single diamond and another that has a causal memory of $\tau = \pm 2L/c$ and depends on the overlap between two causal diamonds.

The cases where only one of the two effects is present, $\eta_1 = 0$ (with $\eta_2 > 0$) and $\eta_2 = 0$ (with $\eta_1 > 0$), have been discussed in previous work [28]. As before, these are the illustrative models that we have physically interpreted as a new kind of exotic “jitter” in space and in beamsplitter position, and used to estimate experimental sensitivity for design purposes.

Similar to the previous class of models, a choice of η_1 and η_2 predicts a frequency spectrum that can be compared with Holometer data, which can be used to generate joint likelihood contours for these two universal parameters.

The parameters are subject to the same constraint that the integral $\int d\tau \Xi$ must be positive:

$$\eta_1 + 4\eta_2 > 0 \quad (20)$$

When the bound is saturated, there is no DC power in the frequency spectrum.

We impose an additional constraint to ensure that Ξ will obtain its maximal value at zero lag:

$$\eta_1 + \eta_2 > 0 \quad (21)$$

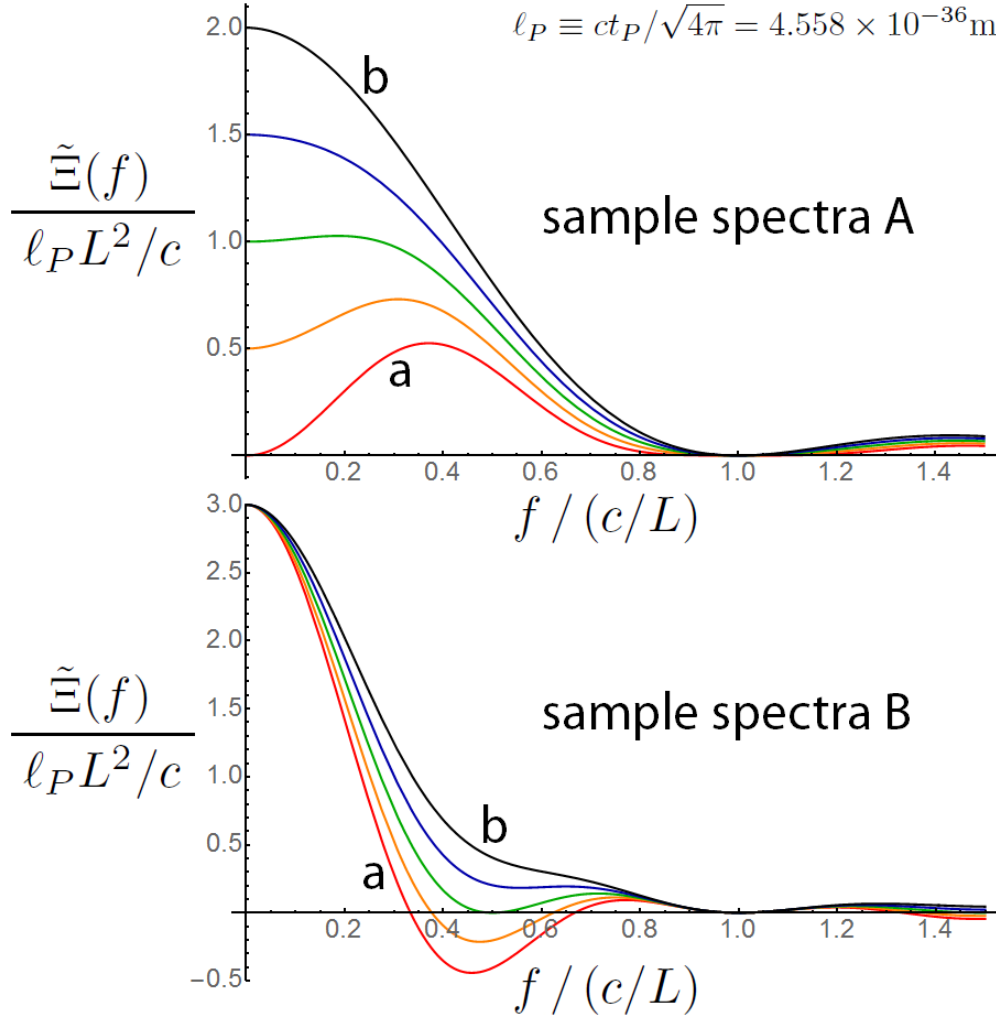


FIG. 7. Models spanning $\pm 2L$: A representative sample of possible frequency domain spectra. Values of η_1 and η_2 are chosen along the two lines labeled “sample spectra” in Figure 8, linearly from “a” to “b.” Vertical axis is scaled relative to ℓ_P . Horizontal axis is scaled to inverse light travel time for L .

This is of course not a sufficient condition without $\eta_1 + 2\eta_2 > 0$, but that will be automatically satisfied by other bounds that we will establish in the normalization section below.

The analytic form of the frequency domain power spectrum is given as:

$$\tilde{\Xi}(f) = 2 \int_0^\infty (\Xi_1(\tau) + \Xi_2(\tau)) \cos(2\pi f\tau) d\tau \quad (22)$$

$$= \frac{2c\eta_1}{(2\pi f)^2} \left[1 - \cos\left(\frac{f}{c/2\pi L}\right) \right] + \frac{2c\eta_2}{(2\pi f)^2} \left[1 - \cos\left(\frac{f}{c/4\pi L}\right) \right] \quad (23)$$

$$= c\eta_1 \left(\frac{L}{c}\right)^2 \text{sinc}^2\left(\frac{f}{c/\pi L}\right) + c\eta_2 \left(\frac{2L}{c}\right)^2 \text{sinc}^2\left(\frac{f}{c/2\pi L}\right) \quad (24)$$

Figure 7 shows a sampling of the type of spectra that are expected. The two plots are a representative sample of the mathematical characteristics featured in $\tilde{\Xi}(f)$ as η_1 and η_2 span the whole range of possible values.

Normalization for Measurable Correlated Noise: Upper and Lower Bounds

As with the previous class of models (spanning $\pm L$), we will use Eq.(14) and a similar set of assumptions to establish benchmark normalizations and upper and lower bounds for η_1 and η_2 .

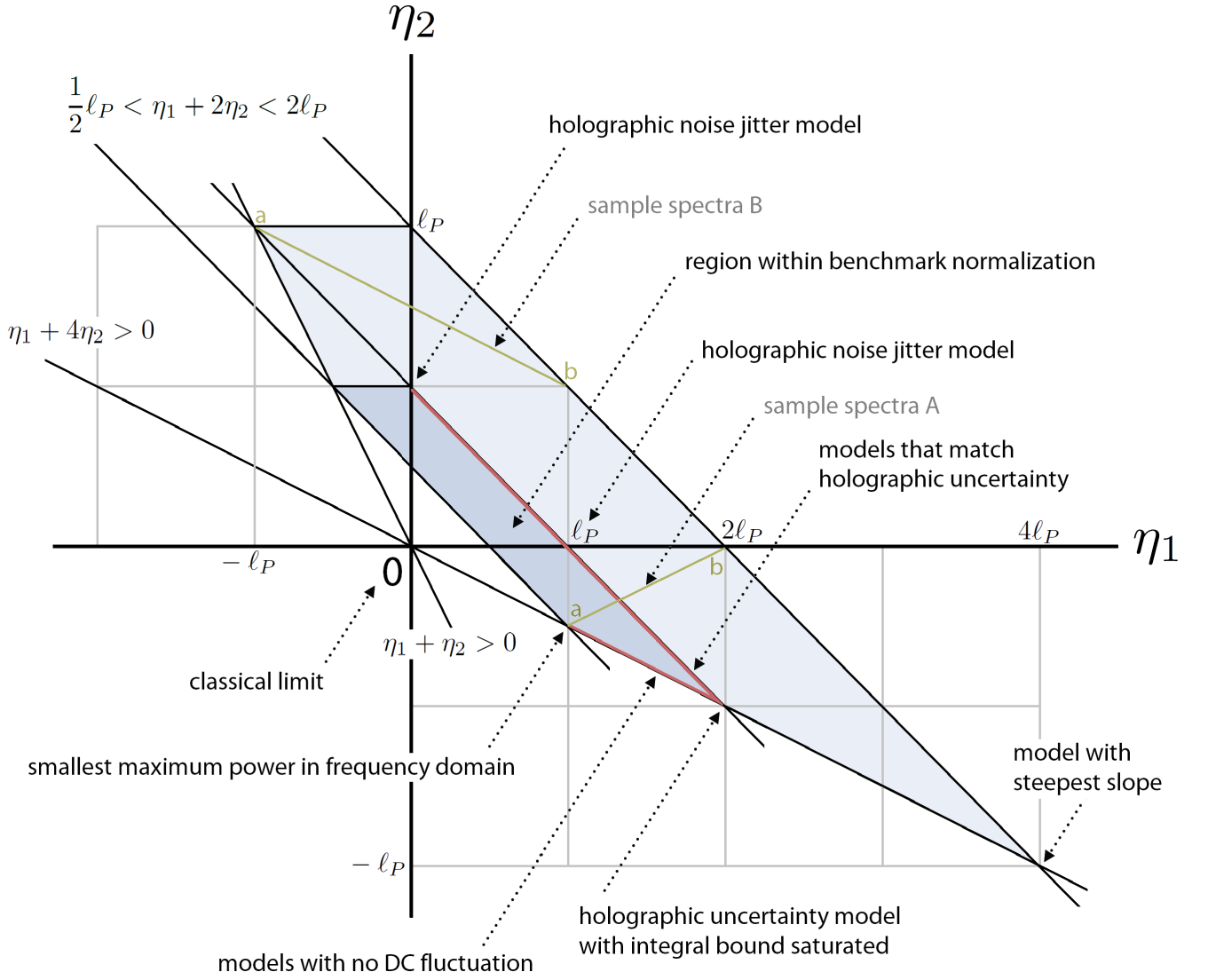


FIG. 8. Models spanning $\pm 2L$: A different set of two observable length parameters spans all possible models of noise that are consistent with symmetries of spacetime, causal structure, and holographic limits on geometric information (the shaded regions). The darker shaded area represents the region of parameter space bounded by our benchmark normalization.

We first note that, similar to the previous class,

$$\frac{1}{2}\ell_P < \Xi(\tau=0)/L = \eta_1 + 2\eta_2 < 2\ell_P. \quad (25)$$

From the upper bound $|\Xi(\tau)| < 2\ell_P L$, we write:

$$|\eta_1| < 4\ell_P \quad \text{and} \quad |\eta_2| < \ell_P \quad (26)$$

Technically, we could allow $\ell_P < |\eta_2| < 2\ell_P$ if η_1 and η_2 are opposite in sign such that $|\eta_1 + 2\eta_2| < 2\ell_P$, but this is a highly unlikely region. We can reasonably expect $|\Xi(\tau = \pm L)| < \ell_P L$ since the amount of overlap between causal diamonds is one-half of its maximum value at zero lag. We will ignore this unlikely possibility.

As before, as our benchmark normalization matching holographic position uncertainty, we use a straightforward comparison between Eq.(14) and $\Xi(\tau=0)/L$:

$$\eta_1 + 2\eta_2 = \ell_P, \quad |\Xi(\tau)| < \ell_P L \quad (27)$$

The region of parameter space allowed within the above constraints is plotted in Figure 8. The Holometer is expected to reach the sensitivity to confirm or reject all physically viable models.

IV. UPPER LIMITS FROM GEO-600 AND PROJECTED SENSITIVITY FOR THE HOLOMETER

Figure 9 demonstrates how these parameter spaces are used to interpret experimental data and draw constraints on different phenomenological models. The two lines labeled “GEO-600 noise” reflect upper limits from [38]. Until high-sensitivity data is available from the Fermilab Holometer, GEO-600, employing a single Michelson interferometer with folded arms, is currently the experiment most sensitive to this type of Planckian geometrical correlation [28]. While it has proven difficult to comprehensively identify and quantify sources of other environmental and technical noise[43], the collaboration has produced a rough upper limit on unidentified flat-spectrum strain noise (the “signal”) around the $1 \sim 6\text{kHz}$ range where shot noise is dominant and can be reliably modeled, at $1.25 \times 10^{-22}\text{Hz}^{-1/2}$ [38]. Because this upper limit is only available in a relatively narrow band at a frequency much lower than c/L (around 0.5MHz for GEO-600), it can only specify one point on the frequency spectrum and corresponds to a straight line in the parameter space. We plot two lines because it is not clear whether the folded arms in GEO-600 would contribute to a twofold increase in the variance measured in differential arm length. Such considerations were discussed in previous work[28], and the nominal models discussed there are plotted as specific points on the parameter space, as illustrative examples.

For the Fermilab Holometer, we have plotted an example contour based on expected noise levels, assuming unity signal-to-noise at the peak of the predicted spectrum corresponding to each point on the contour. This of course assumes that geometry behaves classically up to the level of projected sensitivity referenced by the contour. The only publicly available data from the Holometer is from an early one-hour data run that was used to set limits on gravitational waves at high frequencies[41, 42], but using the behavior of cross-correlated and integrated shot noise described in [28, 39, 40], it is straightforward to extrapolate the noise levels measured in the one-hour data to much longer integration times and different choices for frequency binning [44]. The result is roughly consistent with the theoretically predicted levels of shot noise[28, 39, 40], and should be considered accurate to about $\pm 10\%$ depending on the exact calibration reached in higher-sensitivity data. Because this sensitivity example is available across a much wider range of frequencies ($1 \sim 11\text{MHz}$), we are able to generate contours that cover much wider classes of models that reach maximal power at different frequencies, by choosing a frequency bin of width 0.5MHz around the peak for each modeled spectrum (e.g. Figures 4 and 7).

These contours for the Holometer do not reflect actually measured data, or shot noise-subtracted residual noise like the GEO-600 lines; they are projected estimates of typical contours of unity signal-to-noise based on expected levels of shot noise, extrapolated from early data of much lower sensitivity that is insufficient to detect any Planckian correlation. These contours are meant to demonstrate that in case of a null result, the Holometer has the capacity to rule out all physically allowed regions within these parameter spaces, within reasonable integration times.

V. FUTURE CONFIGURATION POSSIBILITIES

Figure 10 shows the default setup of the Holometer, with two adjacent Michelson interferometers oriented in a nested configuration.

Other configurations of correlated interferometers are possible. By sampling the spacetime differently, they can explore different behaviors of the quantum geometry. Figure 11 shows two significant alternative configuration possibilities. A configuration with the two interferometers oriented back-to-back serves as null control for the default configuration[27] or selects for an exotic form of directional uncertainty in which the two beam splitters, each simultaneously measuring position in two directions, are orthogonal to each other.

The spatially extended Sagnac configuration, also shown in Figure 11, is a particularly interesting future possibility amongst configurations that involve interferometers more complex than a Michelson setup. It would be sensitive to pure rotational correlation modes that are invisible to Michelson systems. This form of symmetry for geometrical correlations might be expected in some theories of quantum geometry.

Even more possibilities are depicted in Figure 12. These include null controls for the nested and back-to-back configurations or the Sagnac; configurations in which the two interferometers are not adjacent to each other, meaning their causal diamonds overlap but do not share almost identical 4-volumes; or setups that involve other complex interferometers. These could be used to test for more exotic types of nonlocal correlations, or serve as more finely tuned detectors in case of a detection in the earlier stages of the experimental program.

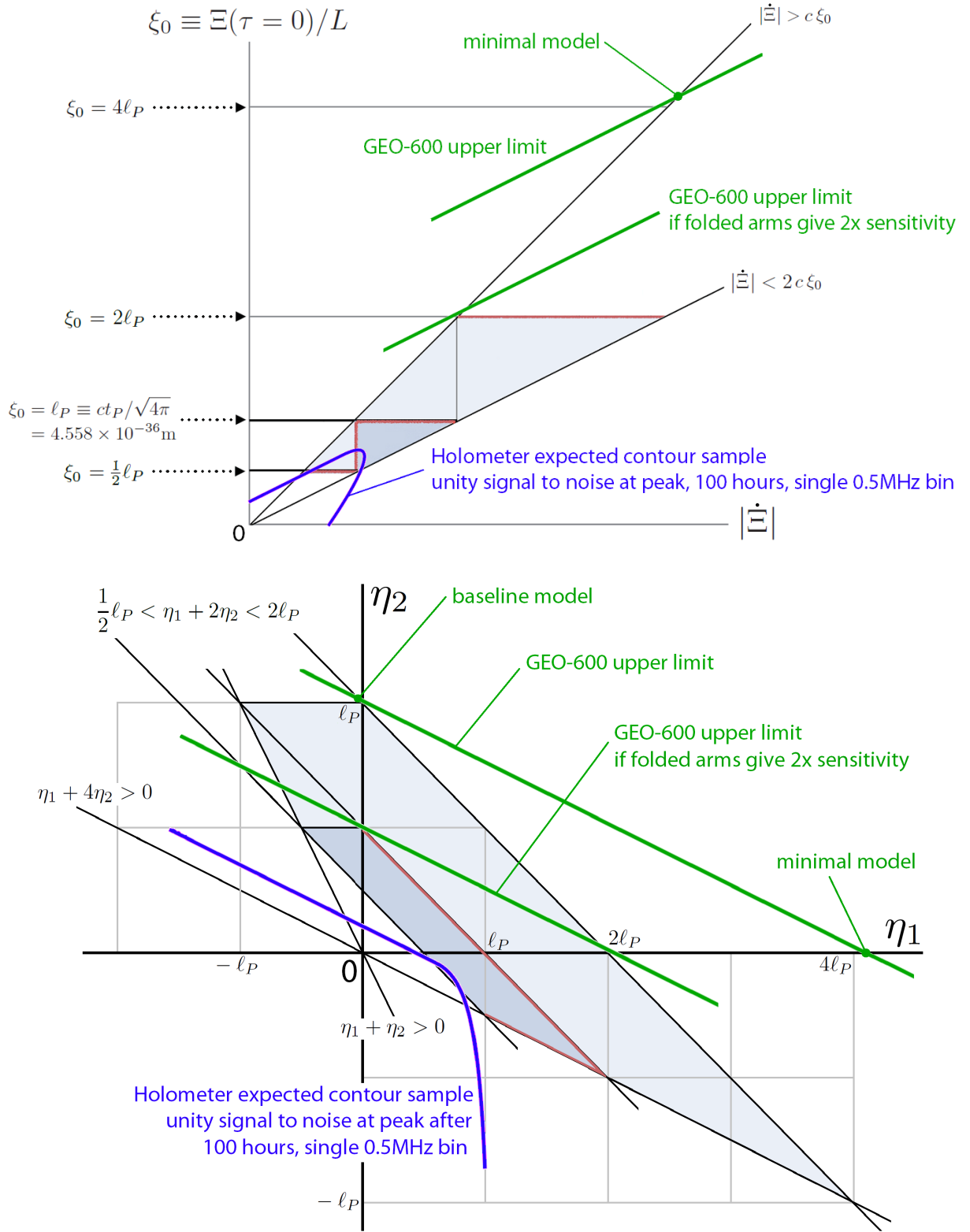


FIG. 9. Upper limits on holographic noise from GEO-600 [38] are given under specific assumptions about whether the folded arms lead to a twofold increase in signal power. The illustrative examples of “minimal model” and “baseline model” refer to [28]. Also shown are projected estimates of contours in future Holometer data, assuming unity signal-to-noise ratio at the peak (accurate to $\pm 10\%$) [28, 39–42]. In the case of a null result, longer integration times would move the contour closer towards the classical limit at the origin. It appears that a highly significant exclusion of the holographic noise hypothesis is possible with a realistic integration time. If there is a detection, the likelihood contour would converge around a single point in the parameter spaces, possibly much farther away from the origin than the plotted examples.

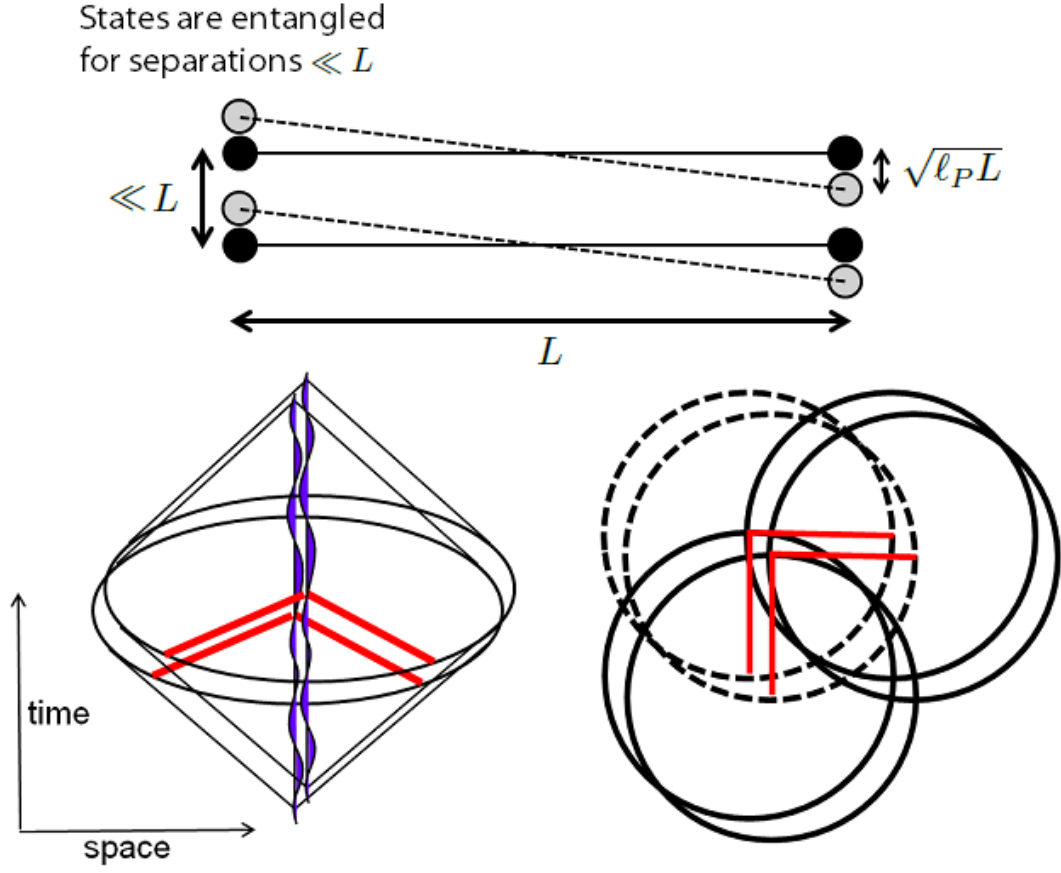


FIG. 10. The default nested configuration of the Holometer.

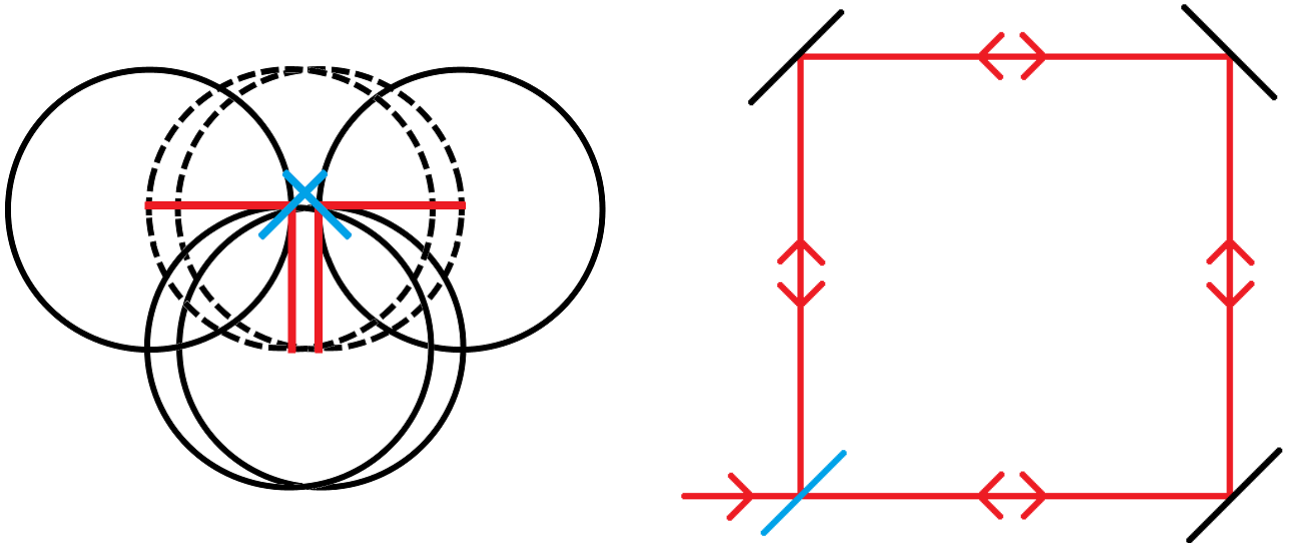


FIG. 11. An alternative configuration with the two adjacent interferometers oriented back-to-back, and a spatially extended Sagnac interferometer.

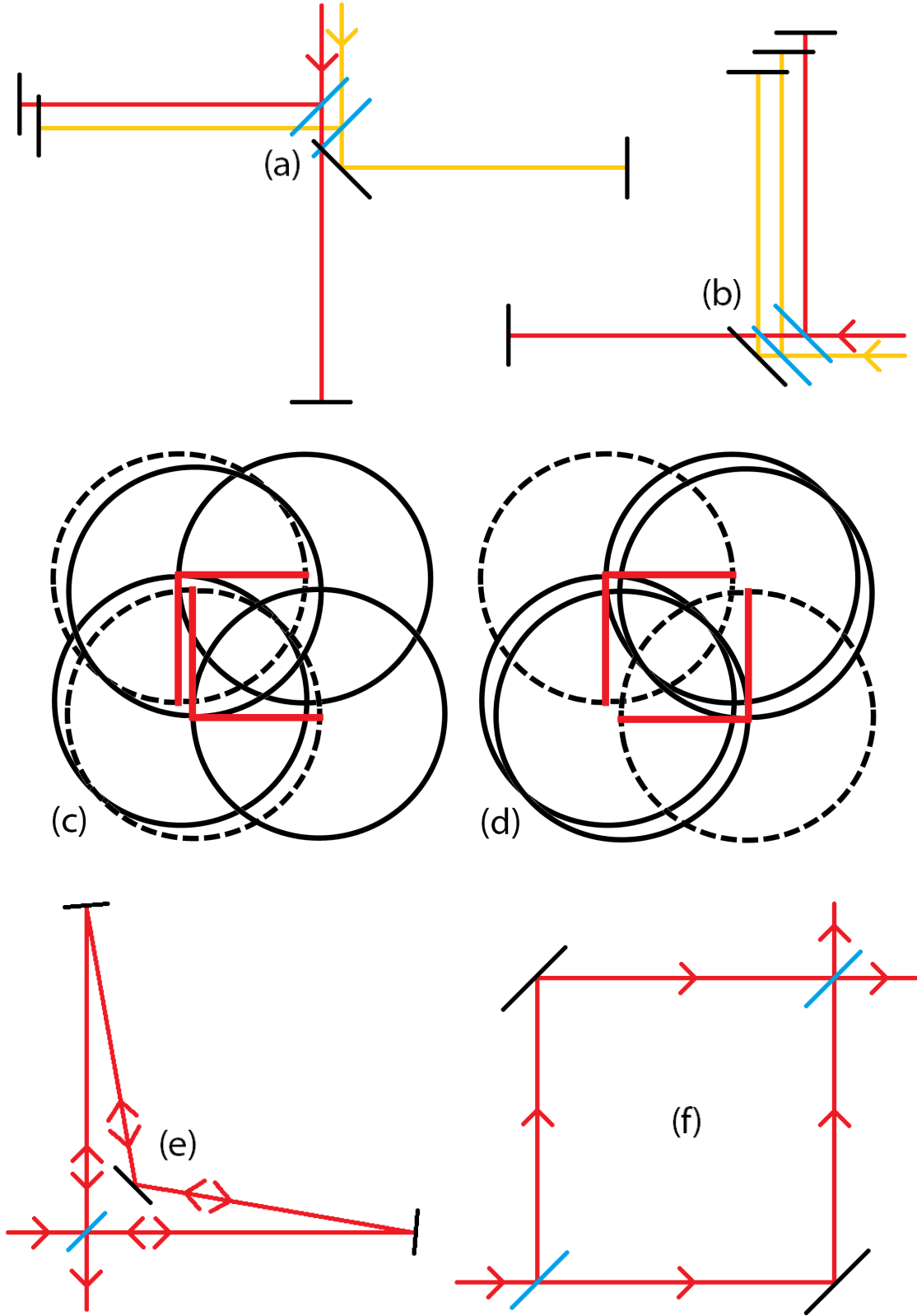


FIG. 12. Possible alternative configurations for correlated interferometers. (a) and (b) are null controls for currently planned configurations. (c) and (d) use two Michelson interferometers whose beamsplitters are not adjacent to each other, and test for exotic types of nonlocal geometric entanglement. (e) and (f) involve interferometers that are differently set up: the zero-area Sagnac interferometer and the Mach-Zender interferometer. These sample the spacetime differently and select for more specific models of geometrical quantum correlation or serve as null controls for some future configurations.

ACKNOWLEDGMENTS

We are grateful to Aaron Chou, Robert Lanza, Stephen Meyer, Lee McCuller, Jon Richardson, Rainer Weiss, Chris Stoughton, and other members of the Holometer team for their detailed inputs on the various aspects of interferometer design, noise behavior, and signal interpretation. We thank Hartmut Grote for his explanations regarding GEO-600 noise models and data interpretation. This work was supported by the Department of Energy at Fermilab under Contract No. DE-AC02-07CH11359, and at the University of Chicago by a grant from the John Templeton Foundation.

-
- [1] C. Rovelli. *Quantum Gravity*. Cambridge University Press, 2004.
 - [2] A. Ashtekar. Introduction to Loop Quantum Gravity. *PoS, QGQGS2011:001*, 2011. arXiv:1201.4598 [gr-qc].
 - [3] S. Deser and P. van Nieuwenhuizen. Nonrenormalizability of the quantized Dirac-Einstein system. *Phys. Rev.*, D10:411, 1974.
 - [4] S. Weinberg. *The Quantum Theory of Fields*. Cambridge University Press, 1996.
 - [5] F. Wilczek. Quantum field theory. *Rev. Mod. Phys.*, 71:S85, 1999.
 - [6] J. Ellis, N. Mavromatos, and D. V. Nanopoulos. String theory modifies quantum mechanics. *Phys. Lett.*, B293:37, 1992.
 - [7] J. Polchinski. *String Theory*. Cambridge University Press, 1998.
 - [8] S. Hossenfelder. Minimal length scale scenarios for quantum gravity. *Living Rev. Rel.*, 16:2, 2013.
 - [9] M. R. Douglas and N. A. Nekrasov. Noncommutative field theory. *Rev. Mod. Phys.*, 73:977, 2001.
 - [10] S. B. Giddings, D. Marolf, and J. B. Hartle. Observables in effective gravity. *Phys. Rev. D*, 74:064018, 2006.
 - [11] S. B. Giddings. Black holes, information, and locality. *Mod. Phys. Lett.*, A22:2949, 2007.
 - [12] T. Banks. Holographic space-time: The takeaway. arXiv:1109.2435 [hep-th], 2011.
 - [13] J. M. Bardeen, B. Carter, and S. Hawking. The four laws of black hole mechanics. *Commun. Math. Phys.*, 31:161, 1973.
 - [14] J. D. Bekenstein. Black holes and entropy. *Phys. Rev.*, D7:2333, 1973.
 - [15] J. D. Bekenstein. Generalized second law of thermodynamics in black-hole physics. *Phys. Rev.*, D9:3292, 1974.
 - [16] S. Hawking. Black hole explosions. *Nature*, 248:30, 1974.
 - [17] S. Hawking. Particle creation by black holes. *Commun. Math. Phys.*, 43:199, 1975.
 - [18] G 't Hooft. Dimensional reduction in quantum gravity. In *Conference on Particle and Condensed Matter Physics (Salam-fest)*, 1993. arXiv:gr-qc/9310026.
 - [19] T. Jacobson. Thermodynamics of spacetime: The Einstein equation of state. *Phys. Rev. Lett.*, 75:1260, 1995.
 - [20] L. Susskind. The world as a hologram. *J. Math. Phys.*, 36:6377, 1995.
 - [21] R. Bousso. The holographic principle. *Rev. Mod. Phys.*, 74:825, 2002.
 - [22] E. Verlinde. On the origin of gravity and the laws of Newton. *JHEP*, 1104:029, 2011.
 - [23] A. G. Cohen, D. B. Kaplan, and A. E. Nelson. Effective field theory, black holes, and the cosmological constant. *Phys. Rev. Lett.*, 82:4971, 1999.
 - [24] C. J. Hogan. Quantum entanglement of matter and geometry in large systems. arXiv:1412.1807 [gr-qc], 2014.
 - [25] C. J. Hogan. Measurement of quantum fluctuations in geometry. *Phys. Rev.*, D77:104031, 2008.
 - [26] C. J. Hogan. Indeterminacy of holographic quantum geometry. *Phys. Rev.*, D78:087501, 2008.
 - [27] C. J. Hogan. Interferometers as probes of Planckian quantum geometry. *Phys. Rev.*, D85:064007, 2012.
 - [28] O. Kwon and C. J. Hogan. Interferometric probes of Planckian quantum geometry. arXiv:1410.8197 [gr-qc], 2014.
 - [29] R. X. Adhikari. Gravitational radiation detection with laser interferometry. *Rev. Mod. Phys.*, 86:121, 2014.
 - [30] URL: <http://holometer.fnal.gov>.
 - [31] T. Banks. Deriving particle physics from quantum gravity: A plan. arXiv:0909.3223 [hep-th], 2009.
 - [32] H. Salecker and E. P. Wigner. Quantum limitations of the measurement of space-time distances. *Phys. Rev.*, 109:571, 1958.
 - [33] C. M. Caves. Quantum-mechanical radiation-pressure fluctuations in an interferometer. *Phys. Rev. Lett.*, 45:75, 1980.
 - [34] C. M. Caves, K. S. Thorne, R. W. P. Drever, V. D. Sandberg, and M. Zimmermann. On the measurement of a weak classical force coupled to a quantum-mechanical oscillator. I. Issues of principle. *Rev. Mod. Phys.*, 52:341, 1980.
 - [35] I. Ruo Berchera, I. P. Degiovanni, S. Olivares, and M. Genovese. Quantum light in coupled interferometers for quantum gravity tests. *Phys. Rev. Lett.*, 110:213601, 2013.
 - [36] A.E. Siegman. *Lasers*. University Science Books, Sausalito, 1986.
 - [37] C. Gardiner and P. Zoller. *Quantum Noise: A Handbook of Markovian and Non-Markovian Quantum Stochastic Methods with Applications to Quantum Optics*. Springer Series in Synergetics. 2004.
 - [38] V. Frolov and H. Grote. Gravitational wave detectors in Europe and the U.S. Fermilab Seminar, April 7, 2014. URL: http://astro.fnal.gov/events/Seminars/Slides/VFrolov_HGrote%20040714.pdf.
 - [39] A. Chou, R. Weiss et al. (Fermilab Holometer Collaboration). The Fermilab Holometer: A program to measure Planck scale indeterminacy. 2009. URL: http://www.fnal.gov/directorate/program_planning/Nov2009PACPublic/holometer-proposal-2009.pdf.
 - [40] B. Kamai et al. (Fermilab Holometer Collaboration). The Fermilab Holometer: Probing the Planck scale. In *Am. Astron. Soc. Meeting #221 #431.06*, 2013.

- [41] R. K. Lanza. *Experimental Limits on Gravitational Waves in the MHz Frequency Range*. PhD thesis, The University of Chicago, 2015. URL: <http://search.proquest.com/docview/1667718530?accountid=14657>.
- [42] R. K. Lanza. Experimental limits on gravitational waves in the MHz frequency range with the Fermilab Holometer. Fermilab Seminar, March 27, 2015. URL: http://theory.fnal.gov/jetp/talks/Lanza_Fermilab_GW_talk_20150327.pdf.
- [43] S. Hild for the GEO-600 Collaboration. Recent experiments in GEO600 regarding the holographic noise hypothesis. Holographic Noise Workshop, Albert Einstein Institute, May 2009. URL: http://www.physics.gla.ac.uk/~shild/presentations/holographic_noise_experiments_GEO600.pdf.
- [44] The cross-correlation analysis in [41, 42] removes one of the two photodetectors in one interferometer, due to concerns about data quality. The cross-interferometer spectrum is the geometric mean of the two single-interferometer sensitivities, so the effect on the final noise level is around $2^{1/4}$. This has been taken into account in generating projected sensitivities.
- [45] C. J. Hogan. A model of macroscopic geometrical uncertainty. arXiv:1204.5948 [gr-qc], 2012.
- [46] A. Connes. *Noncommutative Geometry*. Academic Press, 1994.
- [47] A. Connes and M. Marcolli. A walk in the noncommutative garden. arXiv: math/0601054, 2006.
- [48] N. Seiberg and E. Witten. String theory and noncommutative geometry. *JHEP*, 9909:032, 1999.
- [49] L. D. Landau and E. M. Lifshitz. *Quantum Mechanics: Non-Relativistic Theory*. Pergamon, Oxford, 3rd edition, 1977. Secs 26 & 27.

APPENDIX: NORMALIZATION FROM COMMUTATOR ALGEBRA

Although an approximately Planckian magnitude for wave function spreading is expected using scaling from standard quantum mechanics, it is useful to adopt an exact benchmark value in absolute physical units, based on a particular algebraic system that has both a precisely calculable information content and a precisely calculable position variance. We adopt here the following simple model of a quantum system based on the familiar spin algebra that has these properties, and does not depend on the system dynamics. Of course, just because this model is precise does not mean it is correct. This particular way of counting information[45] is not a necessary assumption for the validity of the generalized framework proposed above, which relies only on first principles such as causal structure and symmetries of spacetime.

1. Covariant Commutation Relations

Suppose that the position of a world-line in each direction μ is a quantum observable, represented by a self-adjoint operator \hat{x}_μ . The commutators of these operators represent the quantum deviations of a body from a classical trajectory, assuming a body massive enough (much greater than the Planck mass) that we can ignore the usual quantum effects associated with its motion.

Consider the following candidate quantum commutator relating position operators in different directions:

$$[\hat{x}_\mu, \hat{x}_\nu] = \hat{x}^\kappa \hat{U}^\lambda \epsilon_{\mu\nu\kappa\lambda} i \ell_P, \quad (28)$$

where indices $\mu, \nu, \kappa, \lambda$ run from 0 to 3 with the usual summation convention, \hat{U} represents an operator with the same form (in the classical limit) as the dimensionless 4-velocity of the body, and $\epsilon_{\mu\nu\lambda\kappa}$ is the antisymmetric 4-tensor. In the limit $\ell_P \rightarrow 0$, the commutator vanishes, and positions in different spatial directions behave independently and classically. If the scale ℓ_P is not zero, there is a finite amount of information.

The explicit dependence adopted in Eq. (28) on position and velocity is driven by the requirement of covariance. The quantum commutator of two vectors requires two antisymmetric indices that must be matched by indices on the right side. Thus we require a nonvanishing antisymmetric tensor, which in four dimensions has four indices, $\epsilon_{\mu\nu\lambda\kappa}$. Two of its antisymmetric indices match those of the noncommuting positions. The other two must contract with two different vectors to avoid vanishing. The geometrically defined options adopted in Eq. (28) are the 4-velocity and position of the body being measured.

Equation (28) is thereby manifestly covariant: the two sides transform in the same way under the homogeneous Lorentz group, as a direct product of vectors. The algebra of the quantum position operators respects the transformation properties of corresponding coordinates in an emergent classical Minkowski space-time, in a limit where the operators are interpreted as the usual space-time coordinates. The model thus defines no preferred direction in space.

On the other hand, Eq. (28) is not translation invariant. The commutator does depend on the position and 4-velocity of the body being measured, or equivalently, on the origin and rest frame of the coordinate system. We interpret this to mean that *the operator \hat{x} describes a quantum relationship between world lines that depends on their relative positions and velocities, but not on any other properties.* The state is defined in relation to a particular world line, the origin of the coordinates. Unlike a classical geometry, which is defined independently of any observer, the state of a quantum geometry is shaped by a relational choice, so it cannot obey translation invariance[1].

It is important to note that Eq. (28) does not define the position operators as “conjugate variables” in the usual sense. In previous work[27] and in standard literature about noncommutative geometry[9, 46–48], a commutator in the form of $[\hat{x}_i, \hat{x}_j] = iC\epsilon_{ij}$ (where ϵ_{ij} is the 2×2 antisymmetric matrix) is used. While Moyal deformations from such an algebra can match the transverse variance generated by Eq. (28) for a Planckian value of the constant C , the relationship to dynamics is clearly different, and the number of states allowed is also different. Most importantly, the standard noncommutative algebra is not covariant, which is why we have adopted Eq. (28).

2. Small Velocity Expansion

A potentially serious problem with Eq. (28) is that quantum 4-velocity operators \hat{U}^λ are not well defined. We can write an expression $\hat{U}^\lambda \equiv \hat{x}^\lambda (\hat{x}_\alpha \hat{x}^\alpha)^{-1/2}$ with the same form (in the classical limit) as the dimensionless 4-velocity of the body, normalized to preserve reparametrization invariance, where $\dot{x} \equiv \partial x / \partial \tau$ and τ denotes proper time. However, a true operator equation should use only the \hat{x}_0 coordinate, not a classical proper time. Although Eq. (28) has a manifestly covariant classical interpretation, we have not proven that it is a consistent operator equation.

We now show that for systems with near-vanishing 4-velocity, there is a 3-dimensional version of the commutator that is a demonstrably consistent quantum algebra. In this limit, it is sufficient for estimating the spatial uncertainty of transverse position. This is analogous to the preparation of states described above in the wave description, with positions measured on constant-time surfaces in the rest frame.

To show that there is a consistent theory at low velocity, expand explicitly the components of Eq. (28). The components of classical 4-velocity are $U = \gamma(1, u_i)$, where $\gamma \equiv (1 - u_i u_i)^{-1/2}$ and $u_i \equiv \partial x_i / \partial x_0 \equiv \partial_t x_i$. Then Eq. (28) breaks into two parts,

$$[\hat{x}_i, \hat{x}_j] = i\gamma(\hat{x}^k \epsilon_{ijk} + \hat{t} \partial_t \hat{x}^k \epsilon_{ijk}) \quad (29)$$

and

$$[\hat{x}_i, \hat{t}] = i\gamma \hat{x}^j \partial_t \hat{x}^k \epsilon_{ijk}, \quad (30)$$

where indices i, j, k now run from 1 to 3, and $\hat{t} \equiv \hat{x}_0$.

Note that we have again adopted a classical time derivative, without explaining its relation to the internally referenced operator quantity, \hat{t} . The appearance of a “time operator” \hat{t} means that in spite of manifest covariance, timelike and null surfaces defined by the operators are frame-dependent. In Eq. (29), an explicit dependence on time coordinate appears, proportional to the velocity. In Eq. (30), a nonzero transverse component of $\partial_t \hat{x}^k$ results in a nonzero commutator of time with the radial component of spatial position, and hence a quantum ambiguity of causal structure. However, both of these terms are suppressed by the 3-velocity, so at low velocity the ambiguity can be neglected.

In laboratory applications on a scale of $\approx 10^{36} \ell_P$, transverse positions spread extremely slowly, at speeds equivalent to about $10^{-18} c$, so the nonrelativistic approximation is excellent. More generally, for a body at rest the terms in Eq. (28) multiplied by 1, 2, 3 components of \hat{U}^λ are smaller in magnitude than the 0 component by a factor of order $|x|^{-1/2}$, which is tiny for a macroscopic system, so they can be consistently neglected. The discussion below is confined to this limit, and thereby avoids confronting the correspondence of \hat{U}^λ with its classical counterpart, or the subtle relationship of the time operator, \hat{x}_0 , with the classical time coordinate.

3. Rest Frame Limit

The physical interpretation of Eq.(28) is most straightforward in the classically defined rest frame of a body, $\partial_t x_i \rightarrow 0$. In that frame, the classical 4-velocity is $U^\lambda = (1, 0, 0, 0)$ so the non-vanishing terms of Eq. (28) are those multiplied by $\epsilon_{\mu\nu\kappa\lambda}$ with $\lambda = 0$. The remaining terms describe a noncommutative geometry in three dimensions:

$$[\hat{x}_i, \hat{x}_j] = \hat{x}_k \epsilon_{ijk} i \ell_P. \quad (31)$$

Eq. (31) describes a quantum-geometrical relationship between positions of two trajectories (or massive bodies) that have proper 3-separation \hat{x}_k , and whose world lines have the same 4-velocity.

The algebra in Eq. (31) defines a consistent quantum theory; indeed, it is the same as the standard quantum description of angular momentum, albeit in an unconventional physical application. Here, position in units of a fundamental length ℓ_P takes the place usually assigned to angular momentum in units of \hbar . The algebra itself is of course well known[49], and leads to precise results on the properties of the quantum system, in this case, a value for the transverse variance of the wave function. The operators in Eq. (31) are well known to obey the Jacobi identities

$$[\hat{x}_i, [\hat{x}_j, \hat{x}_k]] + [\hat{x}_k, [\hat{x}_i, \hat{x}_j]] + [\hat{x}_j, [\hat{x}_k, \hat{x}_i]] = 0, \quad (32)$$

which shows that in the non-relativistic limit (Eq. (31)), the effective quantum theory is self-consistent. Note that this conclusion does not require knowing the commutators for dynamical operators \hat{x}_μ , or knowing the Hamiltonian for the system. Usually, quantum commutators are derived from a correspondence principle with classical Poisson brackets; here, they are motivated just from their symmetries and scaling of information content.

4. Radial Separation Eigenstates

Consider an operator

$$|\hat{x}|^2 \equiv \hat{x}_i \hat{x}_i, \quad (33)$$

corresponding to the squared modulus of separation, analogous to the square of total angular momentum. In the same way that total angular momentum commutes with all of its components, the radial separation between trajectories behaves classically:

$$[\hat{x}^2, \hat{x}_i] = 0, \quad (34)$$

so that emergent causal structure, with light cones defined by $|\hat{x}|^2$, has no quantum uncertainty. For any single direction— for example, a direction of a plane wave mode in field theory— the system behaves classically. It is only in comparison of positions in transverse directions that new quantum-geometric effects appear.

We adapt conventional notation used for angular momentum. Let l denote positive integers corresponding to the quantum numbers of radial separation, analogous to total angular momentum. The separation operator takes discrete eigenvalues:

$$|\hat{x}|^2 |l\rangle = l(l+1)\ell_P^2 |l\rangle. \quad (35)$$

We denote the discrete eigenvalues corresponding to classical separation by

$$L \equiv \sqrt{l(l+1)}\ell_P. \quad (36)$$

It is no accident that such Planckian quantization resembles the spectra for volume and area states more rigorously evaluated within the framework of loop quantum gravity (e.g., [1, 2]). The only advantage of the current approach is that it allows a straightforward exact calculation for geometrical correlations on very large scales.

5. Transverse Wave Function

A body can be in a state of definite radial separation, and also a definite position in any single direction. However, a body cannot be in a definite position state in more than one direction, and this leads to a nonzero variance in the wave function of transverse position. Consider projections of the operator \hat{x}_i . Let l_i denote the eigenvalues of position in direction i . In a state $|l\rangle$ of separation number l , the position operator \hat{x}_i can have eigenvalues in units of ℓ_P ,

$$l_i = l, l-1, \dots, -l, \quad (37)$$

giving $2l+1$ possible values. In an eigenstate with a definite value of position in direction i ,

$$\hat{x}_i |l, l_i\rangle = l_i \ell_P |l, l_i\rangle. \quad (38)$$

Define raising and lowering operators for each direction:

$$\hat{x}_{3\pm} \equiv \hat{x}_1 \pm i\hat{x}_2, \quad (39)$$

with equivalent expressions for cyclic permutations of the indices. These can be used to show[49] that for any i ,

$$|\hat{x}|^2 = \hat{x}_{i+}\hat{x}_{i-} + \hat{x}_i^2 + \hat{x}_i = \hat{x}_{i-}\hat{x}_{i+} - \hat{x}_i^2 + \hat{x}_i. \quad (40)$$

Direct calculation (e.g., ref.[49]) then leads to the following product of amplitudes for measurements of either of the transverse components \hat{x}_j , with $j \neq i$:

$$\langle l_i | \hat{x}_j | l_i - 1 \rangle \langle l_i - 1 | \hat{x}_j | l_i \rangle = (l + l_i)(l - l_i + 1)\ell_P^2/2, \quad (41)$$

again for any i .

The left side of equation (41) can be interpreted as the expected value for the operator

$$\hat{x}_j |l_i - 1\rangle \langle l_i - 1| \hat{x}_j \quad (42)$$

for components with $j \neq i$, in a state $|l_i\rangle$ of definite \hat{x}_i . For $l \gg 1$ and $l_i \approx l$, this corresponds to the expected variance in components of position transverse to separation:

$$\langle \hat{x}_j | l_i - 1 \rangle \langle l_i - 1 | \hat{x}_j \rangle \rightarrow \langle \hat{x}_j^2 \rangle. \quad (43)$$

We conclude that position \hat{x}_\perp in any direction transverse to separation is indeterminate, with a variance given by the right hand side of Eq. (41) in the limit of $l \gg 1$:

$$\langle \hat{x}_\perp^2 \rangle = L\ell_P. \quad (44)$$

Transverse positions show the same quantum indeterminacy as transverse components of angular momentum in the nearly-classical, large-angular-momentum limit. The physical analog is measurement of a component transverse to the angular momentum vector; such a measurement reveals a superposition of transverse direction states, with a range of eigenvalues. In our application, position can similarly have a definite value in the radial direction—corresponding to its classical value—but is indeterminate in the transverse directions. The new quantum-geometrical uncertainty increases with separation, and at macroscopic separations, it is much larger than ℓ_P . Note that the uncertainty in this system cannot be squeezed out of one transverse direction and into another.

6. Number of eigenstates

The geometrical position states have a discrete spectrum. The number of position eigenstates within a 3-sphere of radius R can be counted in the same way as discrete angular momentum eigenstates, as follows.

Recall that radial position has discrete quantum numbers l . Using Eq. (36) with $R = L$, the number l_R of radial position eigenstates for a radius R is given by setting $l_R(l_R + 1) = (R/\ell_P)^2$, that is, they are discrete with approximately Planckian separation. For each of these, from Eq. (37), there are $2l + 1$ eigenstates of direction. The total number of quantum position eigenstates in a 3-sphere is then

$$\mathcal{N}_{Q3S}(R) = \sum_{l=1}^{l_R} (2l + 1) = l_R(l_R + 2) = (R/\ell_P)^2, \quad (45)$$

where the last equality applies in the large l limit. Thus, the number of quantum-geometrical position eigenstates in a volume scales holographically, as the surface area in Planck units.

7. Exact Normalization to Gravity

We can set an absolute physical scale for these relationships from thermodynamics of gravitational systems[19, 22]. The number of states in a 3-sphere can be counted exactly for both geometry and gravity.

The number of position states for a massive body enclosed in a 3-sphere of radius R that statistically reproduces nonrelativistic Newtonian gravity (cf. [22], Eq. 3.10) is given by:

$$\mathcal{N}_{G3S}(R) = 4\pi(R/ct_P)^2, \quad (46)$$

with the usual definition of Planck length, $ct_P \equiv \sqrt{\hbar G/c^3} = 1.616 \times 10^{-35}\text{m}$. Note that this is four times larger than the entropy of a black hole event horizon of the same radius. The quantum-geometrical and gravitational estimates agree, $\mathcal{N}_{Q3S} = \mathcal{N}_{G3S}$, if the numerical value of the effective commutator coefficient ℓ_P is

$$\ell_P = ct_P/\sqrt{4\pi}. \quad (47)$$

If Eq. (47) holds, bodies in the emergent space-time move as described by Newtonian gravity.

From Eq. (44), the theory predicts position variance in physical units,

$$\langle \hat{x}_\perp^2 \rangle = Lct_P/\sqrt{4\pi} = (2.135 \times 10^{-18}\text{m})^2(L/1\text{m}), \quad (48)$$

with no free parameters. The numerical value of the coefficient in Eq. (48) is slightly lower (by a factor of $\sqrt{\pi}/4$) than the value previously estimated by a different method, using a wave theory normalized to black hole entropy (Eq. (29) of ref. [27].) The value computed here is better controlled, because the quantum and gravitational numbers both refer to the same physical system, a spherical 3-volume at rest with no curvature.